

Probing Compact Objects in Wide-Orbit Binaries with Joint LAMOST LRS and MRS

HAO-BIN LIU ¹ AND WEI-MIN GU  ¹

¹*Department of Astronomy, Xiamen University, Xiamen, Fujian 361005, People's Republic of China*

ABSTRACT

Wide-orbit binaries serve as crucial laboratories for understanding stellar evolution and identifying quiescent compact objects. In this work, we search for compact objects in wide-orbit binaries by merging the LAMOST multi-epoch catalogs from LRS and MRS in the 12th data release. We specifically focus on sources with at least 20 observation epochs that clearly exhibit long-term radial velocity (RV) variations while remaining stable over short time scales. By constraining the mass function with Lomb-Scargle periods and RV ranges, we identified 76 single-lined spectroscopic binary candidates harboring potential compact objects with robust orbital solutions. These systems exhibit orbital periods ranging from 10 to 1000 days, with semi-amplitudes of velocity $K_1 \lesssim 50$ km/s and mass functions $f(M_2)$ between 0.05 and $0.6 M_{\odot}$. Combining $f(M_2)$ with SED-derived stellar parameters, we identify 6 strong compact object candidates with main-sequence companions (Class A), 24 systems likely consisting of either compact objects with giant/subgiant companions or mass-inverted Algol-type binaries (Class B), and 46 candidates with relatively lower mass ratios (Class C). Cross-matching with the *Gaia* DR3 `nss_two_star_orbit` catalog yields 16 sources, all of which exhibit orbital solutions consistent with our results. This study demonstrates the essential role of long-term spectroscopic monitoring in searching for compact objects in wide-orbit binaries and validating orbital solutions. The strategy of leveraging extended time baselines will be increasingly effective as spectroscopic databases continue to grow, enabling the systematic discovery of compact objects in wide orbits across the Galaxy.

Keywords: Compact objects (288) — Radial velocity (1332) — Spectroscopic binary stars (1557)

1. INTRODUCTION

Binary systems containing compact objects, such as white dwarfs, neutron stars, or black holes, serve as fundamental laboratories for testing stellar evolution and binary interaction theories. While early investigations into these binaries were mainly shaped by interacting systems characterized by high-energy accretion (B. Warner 1995; R. A. Remillard & J. E. McClintock 2006; D. R. Lorimer 2008; M. J. Middleton et al. 2014), there is a growing consensus on the importance of studying the 'dormant' or quiescent population (T. Yi et al. 2022; Z.-X. Zhang et al. 2022; K. El-Badry et al. 2023; A. Ganguly et al. 2023; P. Nagarajan et al. 2025). Recent advancements in high-precision astrometry, notably from the *Gaia* mission, have successfully unveiled a number of wide-orbit compact object candidates (J. J. Andrews et al. 2022; S. Geier et al. 2023; T. Jayasinghe et al. 2023; K. El-Badry et al. 2024; J. Müller-Horn et al. 2025; C. Y. Lam et al. 2025). These non-accreting systems provide a more unbiased view of binary formation channels.

Complementary to astrometric efforts, multi-epoch spectroscopic surveys have emerged as a powerful tool for exploring this population across a broad range of orbital periods (M. van der Swaelmen et al. 2018; B. Anguiano 2025). In particular, the rich spectral library provided by the Large Sky Area Multi-Object Fiber Spectroscopic Telescope (LAMOST) facilitates a comprehensive search for these hidden objects using RV variations (C. Liu et al. 2020). Our previous work (H.-B. Liu et al. 2024, hereafter L24) revealed 26 compact object candidates in single-lined binaries (SB1) using time-domain spectra from the LAMOST medium-resolution survey (MRS). Subsequent studies have further characterized the nature of the compact object in two notable candidates (X. Zhao et al. 2024a; H. Zhu et al. 2025). However, the L24 selection strategy relied primarily on significant RV variations of the visible companion, specifically focusing on those with an RV difference greater than 100 km/s. Although this approach efficiently identified compact

object binaries, it was naturally biased toward short orbital period systems with large velocity amplitudes (S. Shahaf et al. 2017). As a result, our sample was largely concentrated in the short orbital period regime, with no targets having orbital periods longer than approximately 10 days. This leaves a vast, relatively unexplored parameter space for longer periods, where a significant population of compact objects may still be hidden.

In the present study, we combine LAMOST multi-epoch spectra from MRS and low-resolution survey (LRS), thereby substantially increasing the number of repeated observations for each target. With sufficient repeated measurements, we aim to systematically search for compact objects in long-orbital-period binary systems. The dense temporal coverage allows for well-sampled RV curves of the visible companions, improving sensitivity to systems with long orbital periods. This approach extends previous efforts by enabling exploration of long orbital period compact object candidates that were largely inaccessible in earlier searches. This paper is organized as follows. In Section 2, we describe the data and the methods used to identify candidates. Section 3 presents the main results and the classification of our sample. Finally, we summarize our conclusions and discussion in Section 4.

2. METHOD

2.1. Data Reduction

The MRS spectra have a spectral resolution of $R \sim 7500$, covering the blue wavelength range 4950–5350 Å and the red range 6300–6800 Å, while the LRS spectra have a resolving power of $R \sim 1800$, spanning 3700–9000 Å. LAMOST’s wide field-of-view and multi-fiber design enable large-scale spectroscopic surveys and provide repeated observations for a substantial number of targets (X.-Q. Cui et al. 2012). The LRS dataset contains approximately 12.6 million spectra obtained from 6,602 plates. The MRS dataset includes about 15.5 million spectra, comprising both single-epoch and coadd observations, and offers higher spectral resolution that is well suited for dynamical searches based on RV measurements.

We downloaded the multi-epoch spectroscopic catalogs from LAMOST DR12, including the LRS catalog `dr12_v1.1_LRS_mec.fits.gz` and the MRS catalog `dr12_v1.1_MRS_mec.fits.gz`. To construct a working sample suitable for dynamical searches of compact object binaries, we combined the two catalogs and focused on targets with sufficiently dense temporal sampling. A positional cross-match was performed between the two catalogs within a radius of 2'', allowing repeated observations obtained from both surveys to be associated with individual sources. For each matched source, we calculated the total number of spectroscopic epochs by combining both MRS and LRS measurements. In this study, the MRS data serve as the primary resource for identifying compact object candidates, while the LRS data provide complementary time-domain coverage.

The total number of observations is the first selection criterion. We required each target to have more than 20 spectroscopic epochs in total, combining MRS and LRS observations. This criterion ensures adequate temporal coverage for sampling RV variability, particularly for systems with long orbital periods. Applying this requirement to the combined LAMOST dataset reduced the initial parent sample to a smaller subset of approximately 5×10^4 sources. Additionally, no restrictions were imposed on any catalog parameters, such as spectral type or other stellar properties of the visible companion.

2.2. Candidate Selection

For each source in the combined catalog, we extracted the RV measurements provided by the LAMOST pipeline and constructed a RV series $\{v_{\text{obs},i}\}$. Owing to the large number of spectroscopic epochs available for each target, the orbital phase coverage is generally sufficient. As a result, the maximum observed RV difference $\Delta v_{\text{obs}} = \max(v_{\text{obs},i}) - \min(v_{\text{obs},i})$ can be used as an approximation to twice the RV semi-amplitude, i.e., $\Delta v_{\text{obs}} \simeq 2K$, for the purpose of an initial dynamical assessment.

Using the Lomb–Scargle periodogram (LSP, N. R. Lomb 1976; J. D. Scargle 1981), a preliminary period search was performed on the RV series. The analysis was carried out with the `LombScargle` class implemented in the `astropy.timeseries` module (Astropy Collaboration et al. 2013, 2018, 2022), with the RV series and the corresponding observation times as inputs. Permitted by the multi-year temporal baseline of the data, the period search was optimized for long orbital periods. We set the `minimum_frequency` to $1/10^4 \text{ day}^{-1}$ and the `maximum_frequency` to 1 day^{-1} . This range was chosen to fully exploit the extended temporal coverage of the combined MRS and LRS observations. The highest peak in the LSP was adopted as the candidate period, denoted as P_{LSP} . Based on the P_{LSP}

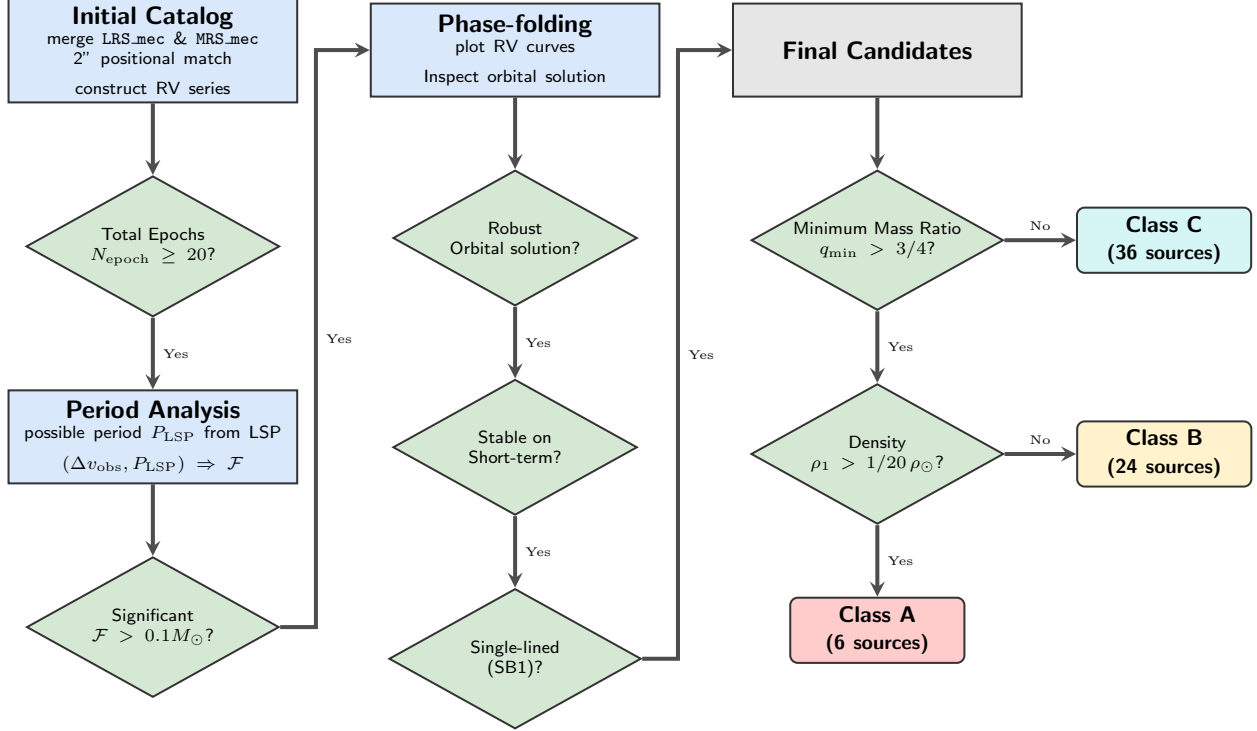


Figure 1. Flowchart of the sample selection and classification process.

obtained from the LSP, we define a mass-function-like screening parameter, denoted as \mathcal{F} , as:

$$\mathcal{F} = 1.013 \times 10^{-7} \left(\frac{\Delta v_{\text{obs}}/2}{\text{km/s}} \right)^3 \left(\frac{P_{\text{LSP}}}{\text{day}} \right) M_{\odot}. \quad (1)$$

As a screening parameter, \mathcal{F} is derived from the observed RV series, $\{v_{\text{obs},i}\}$, and does not represent a true mass function. We applied a threshold on \mathcal{F} , selecting only sources with $\mathcal{F} > 0.1 M_{\odot}$, where this lower limit corresponds to a circular-orbit binary with an inclination of 90° and a mass function of the secondary object equal to $0.1 M_{\odot}$.

The RV series are folded using the corresponding P_{LSP} to construct phase-folded RV curves for remaining sources. Unreasonable RV curves are still produced by the severe deviation between the orbital period P_{orb} and P_{LSP} . Thus RV curves were inspected visually by examining the phase-folded RV curves for coherent orbital modulation. Such discrepancies are likely due to the concentration of observational epochs within limited orbital phases. Systems exhibiting clear and well-defined RV variations consistent with binary orbital motion were readily identified.

Non-uniform temporal sampling always carries the risk of misidentifying the orbital period (J. T. VanderPlas 2018; R. I. Dawson & D. C. Fabrycky 2010). In addition, We examined the original RV series for each candidate. The selected systems are required to show negligible RV variation within a single night or on short timescales (~ 10 days), while exhibiting significant RV changes over longer timescales, consistent with the candidate long orbital periods. This procedure minimizes the likelihood that a system is misclassified as a long-period binary due to limited temporal sampling or short-term variations.

We further identify and exclude double-lined spectroscopic binaries (SB2s). For each source, we visually inspected the available MRS spectra, as they provide sufficient spectral resolution to identify SB2 (M. Kovalev et al. 2022; B. Zhang et al. 2022; Z. Zheng et al. 2023; M. Kovalev et al. 2024; S. Guo et al. 2025). Specifically, the profiles of prominent stellar absorption lines were examined across multiple epochs. We focused on diagnostic absorption features, including H α , Mg I, Ca I, and Fe lines, which are consistently covered within the LAMOST MRS wavelength ranges. We searched for characteristic SB2 signatures such as line splitting, asymmetric absorption profiles, or systematic changes in line shape between different observations, especially when the RV gets its maximum and minimum. Such features indicate the presence of two luminous stellar components contributing to the observed spectrum.

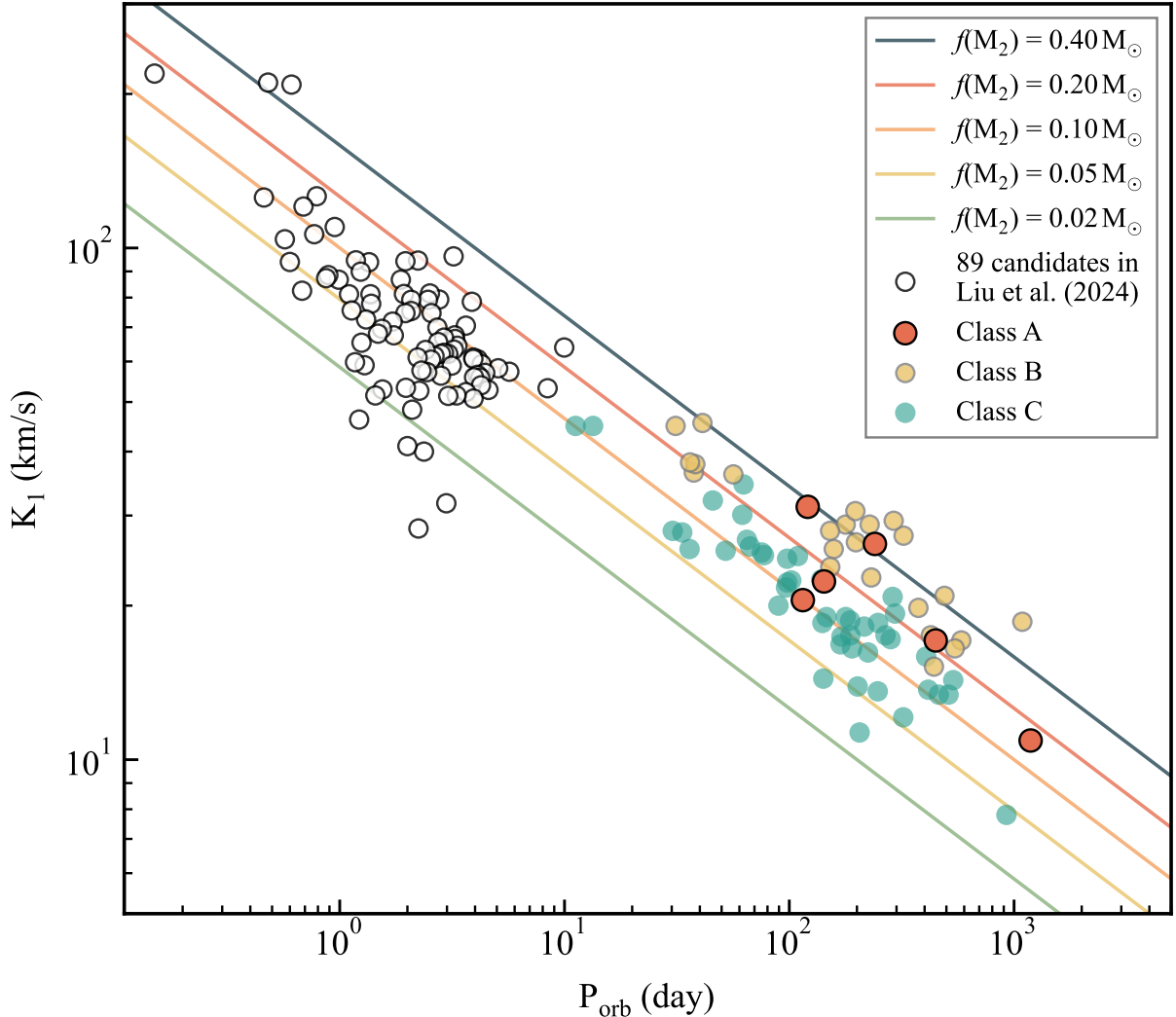


Figure 2. Orbital characteristics of the 76 candidates in the K_1 – P_{orb} plane. Contours of constant mass function $f(M_2)$ (at $e = 0$, from 0.02 to $0.40 M_\odot$) are shown as colored lines. Colored circles indicate our candidates, classified into Class A (orange), B (yellow), and C (teal) according to the criteria described in Section 3.3. These markers are consistent with Figure 3. We show candidates in L24 (white circles) alongside our new candidates. Notably, the L24 candidates are concentrated at significantly shorter orbital periods, whereas our sample extends to longer orbital periods.

3. RESULTS

We selected 76 promising compact object candidates in binaries. These candidates exhibit coherent radial velocity variations consistent with single-lined spectroscopic binary motion and show no detectable signatures of a luminous secondary object in their spectra. As shown in Figure 2, these are promising candidates for the combination of long orbital periods and moderate velocity amplitudes. This population occupies a distinct parameter space compared to the shorter-period systems reported in L24, thereby extending the search for compact objects into the long-period regime.

The orbital parameters of the 76 selected candidates cover a broad range of the parameter space, consistent with a population of wide-separation binaries. The candidate orbital periods are distributed between approximately 10^1 and 10^3 days. We did not prioritize systems with shorter orbital periods. Conversely, the identification of systems with even longer orbital periods is currently constrained by the total duration of the observational baseline. The observed radial velocity semi-amplitudes for these candidates typically range from 10 – 50 km s^{-1} .

3.1. Template Matching

For each of the 76 selected candidates, we derived precise radial velocities through a systematic template-matching procedure. For every target, we prioritized the medium-resolution spectrum with the highest signal-to-noise ratio to serve as the primary reference. To maximize the available spectral information, we spliced the coadded data from the blue and red arms into a single, seamless spectrum.

The matching process was performed utilizing the MARCS synthetic spectral grid in the software `StellarSpecModel` (Z. Zhang 2025a). Three stellar atmospheric parameters (effective temperature, surface gravity and metallicity) were free parameters for the grid interpolator. In addition, rotational velocity and RV are incorporated in the template to ensure the best possible match with the observed line profiles. We employed the `Spectool` software package (Z. Zhang 2025b) to measure the rotational velocities, following a methodology similar to that described in J. Zhuang et al. (2025). To determine the optimal parameter set, we defined the logarithmic likelihood function as follows:

$$\ln \mathcal{L} = -\frac{1}{2} \sum_{i=1}^N \left[\frac{(F_i - F_{m,i}(\theta))^2}{\sigma_i^2} + \ln(2\pi\sigma_i^2) \right], \quad (2)$$

where F_i represents the observed normalized spectral flux, $F_{m,i}(\theta)$ is the synthetic flux generated by the MARCS interpolator for the parameter vector θ , and σ_i is the formal observational uncertainty.

The posterior probability density was sampled using the Markov Chain Monte Carlo ensemble sampler `emcee` (D. Foreman-Mackey et al. 2013). For each candidate, we configured the sampler with a number of walkers equal to four times the number of free parameters. Each walker was evolved for 10,000 steps to ensure thorough convergence and a comprehensive exploration of the parameter space. The final radial velocity for each epoch was adopted from the median of the sampled posterior distribution, with the uncertainties derived from the 16th and 84th percentiles. This rigorous sampling approach ensures that the derived velocities and their associated errors account for the internal degeneracies between the stellar atmospheric properties.

3.2. Orbital Solutions

We derived the radial velocities (RVs) for each epoch across our 76 candidates using the resolution-matched templates. For the MRS, the coadded data from both the blue and red arms were integrated into a single spectral string before performing the cross-correlation. For the low-resolution spectra (LRS), the observed flux was directly cross-correlated against the synthetic templates. To ensure accuracy, all MARCS templates were explicitly downgraded to match the specific instrumental resolution of each observation (either MRS or LRS) prior to the cross-correlation function (CCF) measurement. Then RVs are derived from the CCF module of `Spectool`.

To characterize the dynamical properties of these systems, we fitted the resulting time-series RVs with a Keplerian model. The model predicts the radial velocity at a given time t by numerically solving the Kepler equation $M = E - e \sin E$, where $M = 2\pi(t - t_0)/P_{\text{orb}}$ is the mean anomaly and E is the eccentric anomaly. We implemented a numerical solver (via `scipy.optimize.fsolve`) to determine E , which was subsequently used to calculate the true anomaly θ through the relation $\tan(\theta/2) = \sqrt{(1+e)/(1-e)} \tan(E/2)$. The complete radial velocity model is expressed as:

$$V_r(t) = K_1 \{ \cos[\theta(t) + \omega] + e \cos \omega \} + \gamma, \quad (3)$$

where $\theta(t)$ is calculated as described above, and the model includes six free parameters: the systemic velocity γ , representing the motion of the binary's barycenter relative to the observer; the radial velocity semi-amplitude of the primary star K_1 ; the orbital period P_{orb} ; the eccentricity e , which defines the shape of the orbit; the argument of periastron ω , specifying the orientation of the orbit in the orbital plane; and the time of periastron passage t_0 . We utilized the `scipy.optimize.curve_fit` routine to minimize the residuals between the observed and predicted RVs, deriving the optimal parameter set and their associated 1σ uncertainties from the resulting covariance matrix.

The mass function is related to the masses of the two components and the orbital inclination, which is defined as follows:

$$f(M_2) = \frac{M_2^3 \sin^3 i}{(M_1 + M_2)^2} = \frac{K_1^3 P_{\text{orb}}}{2\pi G} (1 - e^2)^{3/2}, \quad (4)$$

where M_1 is the mass of the optically visible star; M_2 is the mass of the unseen object; i is the inclination, and G is the gravitational constant. Utilizing the best-fit orbital parameters, we calculated the mass function $f(M_2)$ for each system, which serves as a fundamental dynamical constraint on the nature of the unseen object.

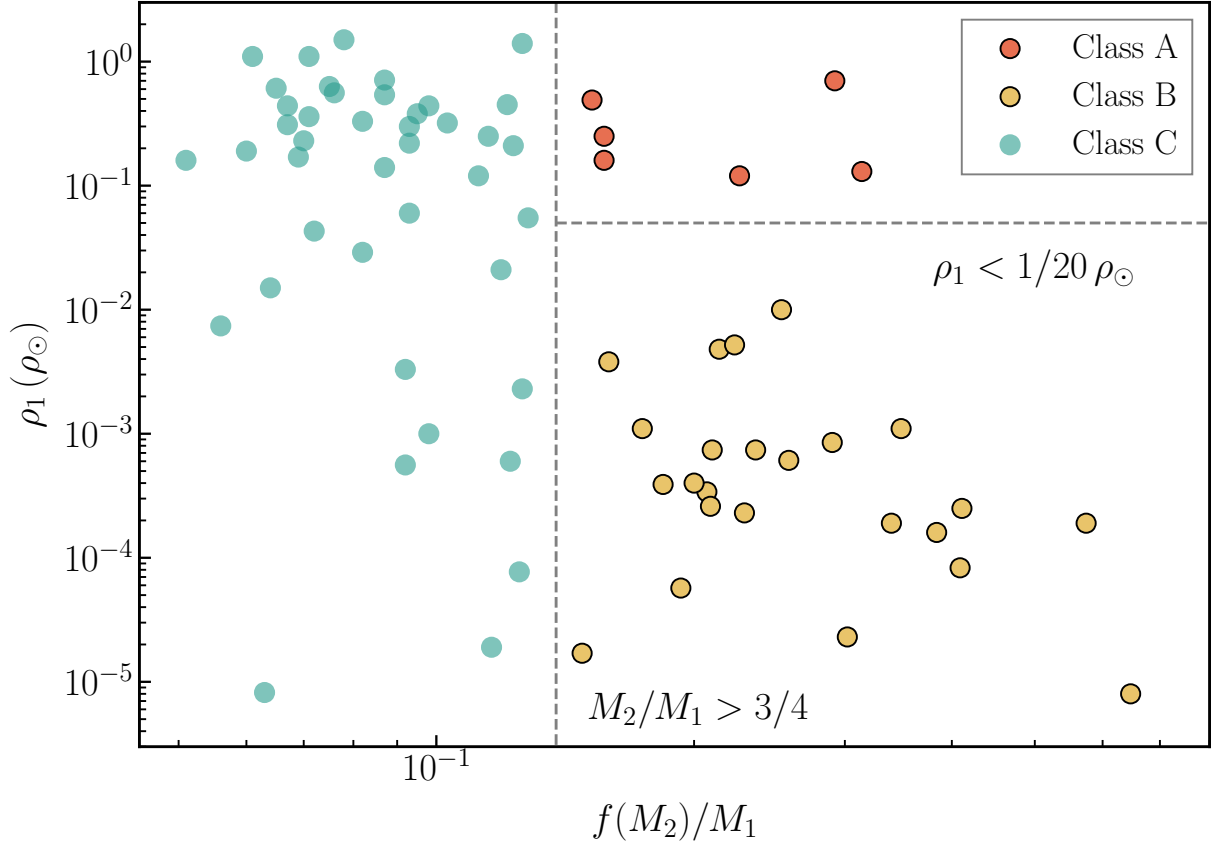


Figure 3. Distribution of the mass function ratio $f(M_2)/M_1$ versus the average density of visible companion ρ_1 for our sample of 76 candidates. We classify our candidates into three distinct categories based on their mass functions, mass ratios, and the evolutionary status of the primary stars. Class A (orange) represents systems with mass functions exceeding $0.138 M_1$ (corresponding to a mass ratio $q = M_2/M_1 > 0.75$) and a primary star mean density $\rho_1 \approx M_1 R_1^{-3} < 1/20 \rho_\odot$; these criteria specifically isolate systems consisting of a main-sequence star and a potentially massive compact companion. Class B (yellow) includes targets that exhibit high mass ratios similar to Class A but are characterized by visible primaries in the post-main-sequence stage, such as subgiants or giants, as inferred from their atmospheric parameters. Finally, Class C (teal) comprises the remaining targets with lower mass functions ($f(M_2)/M_1 \leq 0.138$) or less constrained orbital parameters, typically associated with lower-mass stellar companions.

3.3. Classification of Candidates

To obtain robust stellar parameters, we performed spectral energy distribution (SED) modeling of the observed multi-band photometry using the publicly available SED fitting code ARIADNE (J. I. Vines & J. S. Jenkins 2022). ARIADNE utilizes a Bayesian model-averaging approach to match theoretical atmosphere grids. By integrating the *Gaia* DR3 parallax as a prior to constrain the distance, we derived key stellar parameters including effective temperature (T_{eff}), surface gravity ($\log g$), metallicity ($[\text{Fe}/\text{H}]$), and stellar radius (R_1). These parameters, along with the calculated bolometric luminosity, were subsequently interpolated onto the MESA Isochrones & Stellar Tracks (MIST; A. Dotter 2016; J. Choi et al. 2016; B. Paxton et al. 2011, 2019) stellar models to estimate the mass of the visible primary star (M_1).

Based on the derived stellar and orbital parameters, we classified the 76 candidates into three distinct groups as illustrated in Figure 3. The classification is primarily based on the mass ratio proxy $f(M_2)/M_1$ and the stellar density ρ . We adopted a threshold of $f(M_2)/M_1 = 0.138$ to identify systems with high mass ratios. At a constant orbital inclination, $f(M_2)/M_1$ is positively correlated with the mass ratio $q = M_2/M_1$. Specifically, our adopted threshold of $f(M_2)/M_1 = 0.138$ corresponds to a minimum mass ratio of $q_{\text{min}} \gtrsim 3/4$. This lower limit is reached at $i = 90^\circ$. Systems with $f(M_2)/M_1 < 0.138$ are categorized as Class C (teal circles), representing low-mass ratio binaries.

Table 1. Orbital and Physical Parameters of the Candidates in Class A

LAMOST Designation (J2000)	<i>Gaia</i> DR3 source_id	RUWE	P_{orb} (days)	K_1 (km/s)	$f(M_2)$ (M_{\odot})	T_{eff} (K)	R_1 (R_{\odot})	L_1 (L_{\odot})	M_1 (M_{\odot})	$M_{2,\text{min}}$ (M_{\odot})
(1)	(2)	(3)	(4)	(5)	(6)	(7)	(8)	(9)	(10)	(11)
J060228.6+280758.3	3431326755205579264	1.96	120.8	31.2	0.351	6016	2.03	4.92	1.12	1.26
J084314.4+133049.9	609120272034206208	6.14	1184.9	10.9	0.154	5627	1.58	2.29	0.98	0.78
J084423.8+152520.8	609651611028044544	4.14	448.2	17.1	0.225	4510	2.03	1.54	1.00	0.95
J084437.0+194238.9	661148268907314432	6.38	142.7	22.3	0.155	6007	1.27	1.91	1.02	0.80
J084925.8+111656.9	598890862525288192	2.37	114.9	20.5	0.100	4452	1.58	0.88	0.64	0.51
J085354.6+112346.6	604690752001962880	2.12	240.4	26.4	0.246	4534	1.06	0.43	0.84	0.91

NOTE— Column (1): Target designation; Column (2): *Gaia* DR3 source identifier; Column (3): RUWE from *Gaia* DR3; Columns (4)–(6): Orbital period, RV semi-amplitude, and mass function from orbital solution; Columns (7)–(9): Effective temperature, stellar radius, and bolometric luminosity (L_1) from best-fit SED results; Column (10): Primary mass estimated from isochrone; Column (11): Minimum secondary mass calculated at $i = 90^{\circ}$.

For systems exceeding this mass ratio threshold, we further distinguished them using a density criterion of $\rho_1 = (M_1/M_{\odot})(R_1/R_{\odot})^{-3} \rho_{\odot} \geq 1/20 \rho_{\odot}$. Candidates with $\rho_1 > 1/20 \rho_{\odot}$ are designated as Class A (orange circles), while those with lower densities are labeled Class B (yellow circles). The density criterion serves as an indicator of the visible companion’s evolutionary stage, distinguishing between main-sequence stars and more evolved subgiants or giant stars.

Notably, Class A targets represent the most promising candidates for harboring compact objects. Given that $q > 3/4$ for these systems, if the unseen object were a normal main-sequence star, its luminosity would be sufficient to produce detectable spectral lines or significant continuum contributions in our LAMOST spectra. The absence of such secondary signals in our high-S/N observations strongly suggests that the unseen objects in Class A systems are likely compact objects, such as high-mass white dwarfs or neutron stars. One of our Class A candidates, J060228.6+280758.3, has been firstly identified as a binary consisting of a G-type main-sequence star and a compact companion (X. Zhao et al. 2024b). While specific mass estimates may vary depending on the choice of stellar evolution models, their findings consistently point to a high-mass compact object (exceeding $1.36 M_{\odot}$).

For Class B systems, although the ratio $f(M_2)/M_1$ is relatively large, the relatively lower stellar densities suggest that the visible companions are likely evolved stars, such as subgiants or giants. In these cases, the high luminosity of an evolved companion could potentially mask the spectral signatures of a main-sequence star. Notably, some systems in this group may possess mass ratios $q > 1$. Upon precise determination of the orbital inclination i , Class B targets could be identified either as candidates for compact objects or as Algol-type semi-detached binaries undergoing mass transfer.

Class C systems, characterized by $f(M_2)/M_1 < 0.138$, represent the most ambiguous category in our sample. Due to the low mass function relative to the primary mass, the gravitational influence of the secondary is insufficient to distinguish between a low-mass main-sequence star, a white dwarf, or a high-mass object viewed at a very low orbital inclination. Consequently, while these systems are included in our survey, they remain lower-priority candidates for compact object searches without further constraints from multi-epoch high-resolution spectroscopy or astrometric data.

3.4. *Gaia* Astrometry

Gaia DR3 (Gaia Collaboration et al. 2023) provides the most extensive census of binary stars compiled by the astronomical community to date, delivering orbital solutions derived from astrometric and/or spectroscopic measurements for approximately 3×10^5 stars. (J.-L. Halbwachs et al. 2022; B. Holl et al. 2022). We cross-matched our 76 candidates with the *Gaia* DR3 Non-Single Star (NSS) catalog. There are 16 candidates with available *Gaia* orbital solutions, as summarized in Table 2. For these overlapping sources, the orbital periods derived from our LAMOST time-series RVs are in good agreement with those reported by *Gaia*. According to the *Gaia* `nss_solution_type`, the majority of these systems are classified as SB1 (spectroscopic binaries with a single-lined solution), while two candidates possess astrometric orbital solutions.

Table 2. *Gaia* DR3 Cross-match Results for a Subset of Candidates

LAMOST designation	<i>Gaia</i> DR3 source id	Plx (mas)	RUWE	G_{mag} (mag)	P_{orb} (days)	P_{gaia} (days)	NSS solution type
J030035.2+560301.9	459792402416078080	0.45	2.34	13.20	525.6 ± 4.3	518.1 ± 9.7	SB1
J031324.7+545919.5	447622629760600960	0.49	1.61	10.46	291.4 ± 2.2	294.2 ± 0.9	SB1
J034116.6+492438.1	249599279929183744	0.43	1.22	10.74	490.3 ± 2.1	487.1 ± 1.0	SB1
J035243.1+251621.8	66896456396598400	3.36	5.35	12.00	224.0 ± 1.0	222.5 ± 0.9	AstroSpectroSB1
J041014.9+533012.6	275234290455134336	0.51	1.04	12.43	157.7 ± 0.2	158.0 ± 0.3	SB1
J044741.5+483453.0	255981326450428160	0.77	1.49	11.58	282.9 ± 0.1	284.5 ± 1.0	SB1
J050636.5+483830.8	255290523910817024	0.15	1.02	12.91	227.8 ± 0.3	230.1 ± 1.7	SB1
J055223.9+282946.1	3443195600969981440	0.38	1.27	12.10	56.4 ± 0.1	56.4 ± 0.1	SB1
J060228.6+280758.3	3431326755205579264	2.92	1.96	10.73	120.8 ± 0.1	120.9 ± 0.1	SB1
J084423.8+152520.8	609651611028044544	1.67	4.14	13.52	448.2 ± 2.6	451.9 ± 2.5	Orbital
J084437.0+194238.9	661148268907314432	5.76	6.38	10.34	142.7 ± 0.1	142.8 ± 0.1	AstroSpectroSB1
J084925.8+111656.9	598890862525288192	3.79	2.37	10.88	114.9 ± 0.2	114.7 ± 0.2	SB1
J091705.6+415450.4	816137661341669760	1.98	1.16	12.37	109.3 ± 0.3	110.2 ± 0.4	SB1
J114552.7+351726.7	4031997035561149824	1.36	1.27	12.34	138.8 ± 0.2	140.1 ± 0.3	SB1
J142728.2+453124.5	1494473388638937728	1.04	1.79	12.31	536.4 ± 5.6	527.4 ± 5.2	SB1
J142728.2+453124.5	1494473388638937728	1.04	1.79	12.31	536.4 ± 5.6	511.2 ± 4.7	Orbital
J230707.0+352452.3	1914890969694599296	1.01	1.09	12.23	11.2 ± 0.1	11.2 ± 0.1	SB1
J084314.4+133049.9	609120272034206208	1.89	6.14	12.55	1184.9 ± 13.8	---	SecondDegreeTrendSB1

Notes. P_{orb} is the orbital period derived from our LAMOST RV analysis. P_{gaia} is the period from the *Gaia* DR3 NSS catalog. Plx and RUWE are collected from the main *Gaia* source catalog. SB1, Orbital, and AstroSpectroSB1 solutions are retrieved from the `nss_two_body_orbit` table, while the Trend (SecondDegreeTrendSB1) solution is obtained from the `nss_non_linear_spectro` table.

Notably, one specific candidate, J084314.4+133049.9, is classified with a SecondDegreeTrendSB1 solution in the `gaiadr3.nss_non_linear_spectro` table, further characterized by a significantly high RUWE of approximately 6.14. Such an elevated RUWE value underscores the fact that the astrometric measurements are poorly described by a single-star model, strongly suggesting the presence of an unresolved companion. The identification of an acceleration solution for this source provides critical independent support for our derived long-period orbital solution ($P_{\text{orb}} \approx 1184.9$ days); since the orbital period substantially exceeds the *Gaia* DR3 observational baseline, the astrometric signature naturally manifests as a non-linear acceleration trend rather than a closed orbital solution.

4. CONCLUSIONS AND DISCUSSION

In this work, we searched for compact objects in wide-orbit binaries by merging the LAMOST DR12 LRS and MRS multi-epoch catalogs. We identified 76 binary candidates with robust orbital solutions from a sample of sources with at least 20 observation epochs. These systems exhibit orbital periods ranging from 10 to 1000 days, with velocity semi-amplitudes $K_1 \lesssim 50$ km/s and mass functions $f(M_2)$ between 0.05 and $0.6 M_{\odot}$. The selection process, as detailed in Figure 1, relied on identifying long-term radial velocity variations while ensuring stability over short time scales and excluding double-lined spectroscopic binaries.

For each candidate, we determined stellar parameters (T_{eff} , R_1 , $\log g$, and [Fe/H]) through SED fitting and estimated isochrone masses (M_1). Based on the derived $f(M_2)$, M_1 , and R_1 , the 76 candidates were classified into three categories: Class A includes 6 strong compact object candidates with main-sequence companions; Class B consists of 24 binaries with giant or subgiant companions; and Class C contains 46 systems with lower mass ratios.

Gaia DR3 `nss_two_star_orbit` catalog provides 16 candidates with orbital solutions, all of which show consistency with our RV-based results. These findings demonstrate that long-term spectroscopic monitoring, particularly through surveys like LAMOST, is highly effective for uncovering the population of wide-orbit binaries and potential compact object hosts.

Further constraining the mass of the compact object requires the determination of the orbital inclination i . For the majority of our candidates, precisely constraining the stellar rotational velocity is challenging, which limits our ability to derive the inclination from $(v \sin i)$ measurement. Furthermore, in these long-period systems, the visible companions are far from filling their Roche lobes; consequently, the absence of significant ellipsoidal variations in their light curves precludes the use of photometric modeling to constrain the inclination. While targets with Thiele-Innes

elements from *Gaia* provide some initial constraints, the issue of orbital inclination is expected to be more robustly addressed as more epoch astrometry becomes available in future *Gaia* data releases.

The candidate selection in this study exhibits a potential concentration toward late-type stars (spectral types F to M), a distribution that originates from fundamental physical and observational constraints rather than merely the properties of the parent catalog. A primary driver is the necessity for high-precision RV measurements to resolve the subtle modulations characteristic of long-period orbits, where velocity semi-amplitudes are typically small. Late-type stars possess relatively cool stellar atmospheres with a high density of narrow metallic absorption lines, which significantly enhance the signal-to-noise ratio of the CCF. In contrast, early-type stars often feature sparse spectra and significant line broadening due to high rotational velocities or thermal effects, making them less suitable for detecting low-amplitude RV variations. Consequently, these late-type stars serve as the most reliable dynamical tracers for identifying wide-separation, long-period systems.

Finally, the survival and detection of such systems are influenced by the formation history of the compact object. Middle-to-low mass stars, which comprise the majority of our late-type sample, have significantly longer main-sequence lifetimes compared to massive stars, providing a much broader temporal window for observation. Moreover, the formation of a compact object through a supernova event in a massive binary often involves a significant mass loss and a natal kick that can disrupt wide-orbit systems. Systems that remain bound with a late-type companion often represent a population that has survived these dynamical perturbations. Thus, the composition of our sample reflects a combination of the precision required for radial velocity monitoring and the physical conditions necessary for the survival of wide-separation binaries in the Milky Way Galaxy.

ACKNOWLEDGMENTS

We thank Tuan Yi and Xinlin Zhao for the helpful discussion. This work was supported by the National Key R&D Program of China under grants 2021YFA1600401 and 2023YFA1607901, the National Natural Science Foundation of China under grants 12433007 and 12221003. This paper uses the data from the LAMOST survey. Guoshoujing Telescope (the Large Sky Area Multi-Object Fiber Spectroscopic Telescope LAMOST) is a National Major Scientific Project built by the Chinese Academy of Sciences. Funding for the project has been provided by the National Development and Reform Commission. LAMOST is operated and managed by the National Astronomical Observatories, Chinese Academy of Sciences.

Software: Astropy (Astropy Collaboration et al. 2013, 2018, 2022), Emcee (D. Foreman-Mackey et al. 2013), StellarSpecModel (Z. Zhang 2025a), Spectool (Z. Zhang 2025b), ARIADNE (J. I. Vines & J. S. Jenkins 2022), Isochrones (B. Paxton et al. 2015), MultiNest (F. Feroz & M. P. Hobson 2008; F. Feroz et al. 2009, 2019), PyMultinest (J. Buchner et al. 2014)

REFERENCES

Andrews, J. J., Taggart, K., & Foley, R. 2022, arXiv e-prints, arXiv:2207.00680, doi: [10.48550/arXiv.2207.00680](https://doi.org/10.48550/arXiv.2207.00680)

Anguiano, B. 2025, arXiv e-prints, arXiv:2512.15904, doi: [10.48550/arXiv.2512.15904](https://doi.org/10.48550/arXiv.2512.15904)

Astropy Collaboration, Robitaille, T. P., Tollerud, E. J., et al. 2013, A&A, 558, A33, doi: [10.1051/0004-6361/201322068](https://doi.org/10.1051/0004-6361/201322068)

Astropy Collaboration, Price-Whelan, A. M., Sipőcz, B. M., et al. 2018, AJ, 156, 123, doi: [10.3847/1538-3881/aabc4f](https://doi.org/10.3847/1538-3881/aabc4f)

Astropy Collaboration, Price-Whelan, A. M., Lim, P. L., et al. 2022, ApJ, 935, 167, doi: [10.3847/1538-4357/ac7c74](https://doi.org/10.3847/1538-4357/ac7c74)

Buchner, J., Georgakakis, A., Nandra, K., et al. 2014, A&A, 564, A125, doi: [10.1051/0004-6361/201322971](https://doi.org/10.1051/0004-6361/201322971)

Choi, J., Dotter, A., Conroy, C., et al. 2016, ApJ, 823, 102, doi: [10.3847/0004-637X/823/2/102](https://doi.org/10.3847/0004-637X/823/2/102)

Cui, X.-Q., Zhao, Y.-H., Chu, Y.-Q., et al. 2012, Research in Astronomy and Astrophysics, 12, 1197, doi: [10.1088/1674-4527/12/9/003](https://doi.org/10.1088/1674-4527/12/9/003)

Dawson, R. I., & Fabrycky, D. C. 2010, ApJ, 722, 937, doi: [10.1088/0004-637X/722/1/937](https://doi.org/10.1088/0004-637X/722/1/937)

Dotter, A. 2016, ApJS, 222, 8, doi: [10.3847/0067-0049/222/1/8](https://doi.org/10.3847/0067-0049/222/1/8)

El-Badry, K., Rix, H.-W., Quataert, E., et al. 2023, MNRAS, 518, 1057, doi: [10.1093/mnras/stac3140](https://doi.org/10.1093/mnras/stac3140)

El-Badry, K., Rix, H.-W., Latham, D. W., et al. 2024, The Open Journal of Astrophysics, 7, 58, doi: [10.33232/001c.121261](https://doi.org/10.33232/001c.121261)

Feroz, F., & Hobson, M. P. 2008, MNRAS, 384, 449, doi: [10.1111/j.1365-2966.2007.12353.x](https://doi.org/10.1111/j.1365-2966.2007.12353.x)

Feroz, F., Hobson, M. P., & Bridges, M. 2009, MNRAS, 398, 1601, doi: [10.1111/j.1365-2966.2009.14548.x](https://doi.org/10.1111/j.1365-2966.2009.14548.x)

Feroz, F., Hobson, M. P., Cameron, E., & Pettitt, A. N. 2019, The Open Journal of Astrophysics, 2, 10, doi: [10.21105/astro.1306.2144](https://doi.org/10.21105/astro.1306.2144)

Foreman-Mackey, D., Hogg, D. W., Lang, D., & Goodman, J. 2013, PASP, 125, 306, doi: [10.1086/670067](https://doi.org/10.1086/670067)

Gaia Collaboration, Vallenari, A., Brown, A. G. A., et al. 2023, A&A, 674, A1, doi: [10.1051/0004-6361/202243940](https://doi.org/10.1051/0004-6361/202243940)

Ganguly, A., Nayak, P. K., & Chatterjee, S. 2023, ApJ, 954, 4, doi: [10.3847/1538-4357/ace42f](https://doi.org/10.3847/1538-4357/ace42f)

Geier, S., Dorsch, M., Dawson, H., et al. 2023, A&A, 677, A11, doi: [10.1051/0004-6361/202346407](https://doi.org/10.1051/0004-6361/202346407)

Guo, S., Kovalev, M., Li, J., et al. 2025, ApJS, 278, 46, doi: [10.3847/1538-4365/added1](https://doi.org/10.3847/1538-4365/added1)

Halbwachs, J.-L., Pourbaix, D., Arenou, F., et al. 2022, arXiv e-prints, arXiv:2206.05726. <https://arxiv.org/abs/2206.05726>

Holl, B., Sozzetti, A., Sahlmann, J., et al. 2022, arXiv e-prints, arXiv:2206.05439. <https://arxiv.org/abs/2206.05439>

Jayasinghe, T., Rowan, D. M., Thompson, T. A., Kochanek, C. S., & Stanek, K. Z. 2023, MNRAS, 521, 5927, doi: [10.1093/mnras/stad909](https://doi.org/10.1093/mnras/stad909)

Kovalev, M., Chen, X., & Han, Z. 2022, MNRAS, 517, 356, doi: [10.1093/mnras/stac2513](https://doi.org/10.1093/mnras/stac2513)

Kovalev, M., Zhou, Z., Chen, X., & Han, Z. 2024, MNRAS, 527, 521, doi: [10.1093/mnras/stad3222](https://doi.org/10.1093/mnras/stad3222)

Lam, C. Y., Simon, J. D., El-Badry, K., et al. 2025, arXiv e-prints, arXiv:2510.17746, doi: [10.48550/arXiv.2510.17746](https://doi.org/10.48550/arXiv.2510.17746)

Liu, C., Fu, J., Shi, J., et al. 2020, arXiv e-prints, arXiv:2005.07210, doi: [10.48550/arXiv.2005.07210](https://doi.org/10.48550/arXiv.2005.07210)

Liu, H.-B., Gu, W.-M., Zhang, Z.-X., et al. 2024, ApJ, 969, 114, doi: [10.3847/1538-4357/ad4c6f](https://doi.org/10.3847/1538-4357/ad4c6f)

Lomb, N. R. 1976, Ap&SS, 39, 447, doi: [10.1007/BF00648343](https://doi.org/10.1007/BF00648343)

Lorimer, D. R. 2008, Living Reviews in Relativity, 11, 8, doi: [10.12942/lrr-2008-8](https://doi.org/10.12942/lrr-2008-8)

Middleton, M. J., Walton, D. J., Roberts, T. P., & Heil, L. 2014, MNRAS, 438, L51, doi: [10.1093/mnrasl/slt157](https://doi.org/10.1093/mnrasl/slt157)

Müller-Horn, J., Rix, H.-W., El-Badry, K., et al. 2025, arXiv e-prints, arXiv:2510.05982, doi: [10.48550/arXiv.2510.05982](https://doi.org/10.48550/arXiv.2510.05982)

Nagarajan, P., El-Badry, K., Reggiani, H., et al. 2025, PASP, 137, 094202, doi: [10.1088/1538-3873/adfffb7](https://doi.org/10.1088/1538-3873/adfffb7)

Paxton, B., Bildsten, L., Dotter, A., et al. 2011, ApJS, 192, 3, doi: [10.1088/0067-0049/192/1/3](https://doi.org/10.1088/0067-0049/192/1/3)

Paxton, B., Marchant, P., Schwab, J., et al. 2015, ApJS, 220, 15, doi: [10.1088/0067-0049/220/1/15](https://doi.org/10.1088/0067-0049/220/1/15)

Paxton, B., Smolec, R., Schwab, J., et al. 2019, ApJS, 243, 10, doi: [10.3847/1538-4365/ab2241](https://doi.org/10.3847/1538-4365/ab2241)

Remillard, R. A., & McClintock, J. E. 2006, ARA&A, 44, 49, doi: [10.1146/annurev.astro.44.051905.092532](https://doi.org/10.1146/annurev.astro.44.051905.092532)

Scargle, J. D. 1981, ApJS, 45, 1, doi: [10.1086/190706](https://doi.org/10.1086/190706)

Shahaf, S., Mazeh, T., & Faigler, S. 2017, MNRAS, 472, 4497, doi: [10.1093/mnras/stx2257](https://doi.org/10.1093/mnras/stx2257)

van der Swaelmen, M., Merle, T., van Eck, S., Jorissen, A., & Zwitter, T. 2018, in IAU Symposium, Vol. 330, Astrometry and Astrophysics in the Gaia Sky, ed. A. Recio-Blanco, P. de Laverny, A. G. A. Brown, & T. Prusti, 350–351, doi: [10.1017/S1743921317006767](https://doi.org/10.1017/S1743921317006767)

VanderPlas, J. T. 2018, ApJS, 236, 16, doi: [10.3847/1538-4365/aab766](https://doi.org/10.3847/1538-4365/aab766)

Vines, J. I., & Jenkins, J. S. 2022, MNRAS, 513, 2719, doi: [10.1093/mnras/stac956](https://doi.org/10.1093/mnras/stac956)

Warner, B. 1995, Cataclysmic variable stars, Vol. 28

Yi, T., Gu, W.-M., Zhang, Z.-X., et al. 2022, Nature Astronomy, 6, 1203, doi: [10.1038/s41550-022-01766-0](https://doi.org/10.1038/s41550-022-01766-0)

Zhang, B., Jing, Y.-J., Yang, F., et al. 2022, ApJS, 258, 26, doi: [10.3847/1538-4365/ac42d1](https://doi.org/10.3847/1538-4365/ac42d1)

Zhang, Z. 2025a, v1.0.0 Zenodo, doi: [10.5281/zenodo.15109587](https://doi.org/10.5281/zenodo.15109587)

Zhang, Z. 2025b, v1.0.1 Zenodo, doi: [10.5281/zenodo.14947417](https://doi.org/10.5281/zenodo.14947417)

Zhang, Z.-X., Zheng, L.-L., Gu, W.-M., et al. 2022, ApJ, 933, 193, doi: [10.3847/1538-4357/ac75b6](https://doi.org/10.3847/1538-4357/ac75b6)

Zhao, X., Wang, S., Wang, P., et al. 2024a, ApJ, 977, 245, doi: [10.3847/1538-4357/ad9273](https://doi.org/10.3847/1538-4357/ad9273)

Zhao, X., Mu, H., Wang, S., et al. 2024b, ApJ, 964, 101, doi: [10.3847/1538-4357/aced95](https://doi.org/10.3847/1538-4357/aced95)

Zheng, Z., Cao, Z., Deng, H., et al. 2023, ApJS, 266, 18, doi: [10.3847/1538-4365/acc94e](https://doi.org/10.3847/1538-4365/acc94e)

Zhu, H., Wang, W., Li, X., Li, J.-j., & Tian, P. 2025, Journal of High Energy Astrophysics, 45, 428, doi: [10.1016/j.jheap.2025.01.015](https://doi.org/10.1016/j.jheap.2025.01.015)

Zhuang, J., Zhang, Z.-X., Gu, W.-M., & Qi, S. 2025, ApJ, 986, 34, doi: [10.3847/1538-4357/adcf91](https://doi.org/10.3847/1538-4357/adcf91)

APPENDIX

A. ILLUSTRATIVE ORBITAL SOLUTIONS

In this section, we present a selection of RV orbital solutions for nine representative candidates from our sample. Each panel in Figure 4 displays the phase-folded RV curve for a single candidate, along with its best-fit Keplerian orbital solution. The uncertainties for the radial velocity measurements were determined through Monte Carlo simulations to ensure statistical reliability. To derive the orbital solutions, we employed a Markov Chain Monte Carlo approach to fit the key parameters, including the orbital period P_{orb} and the velocity semi-amplitude K_1 . The detailed orbital parameters for these and all other candidates are comprehensively listed in Tables 1, 3 and 4 (for Class A, B and C, respectively) in Appendix C.

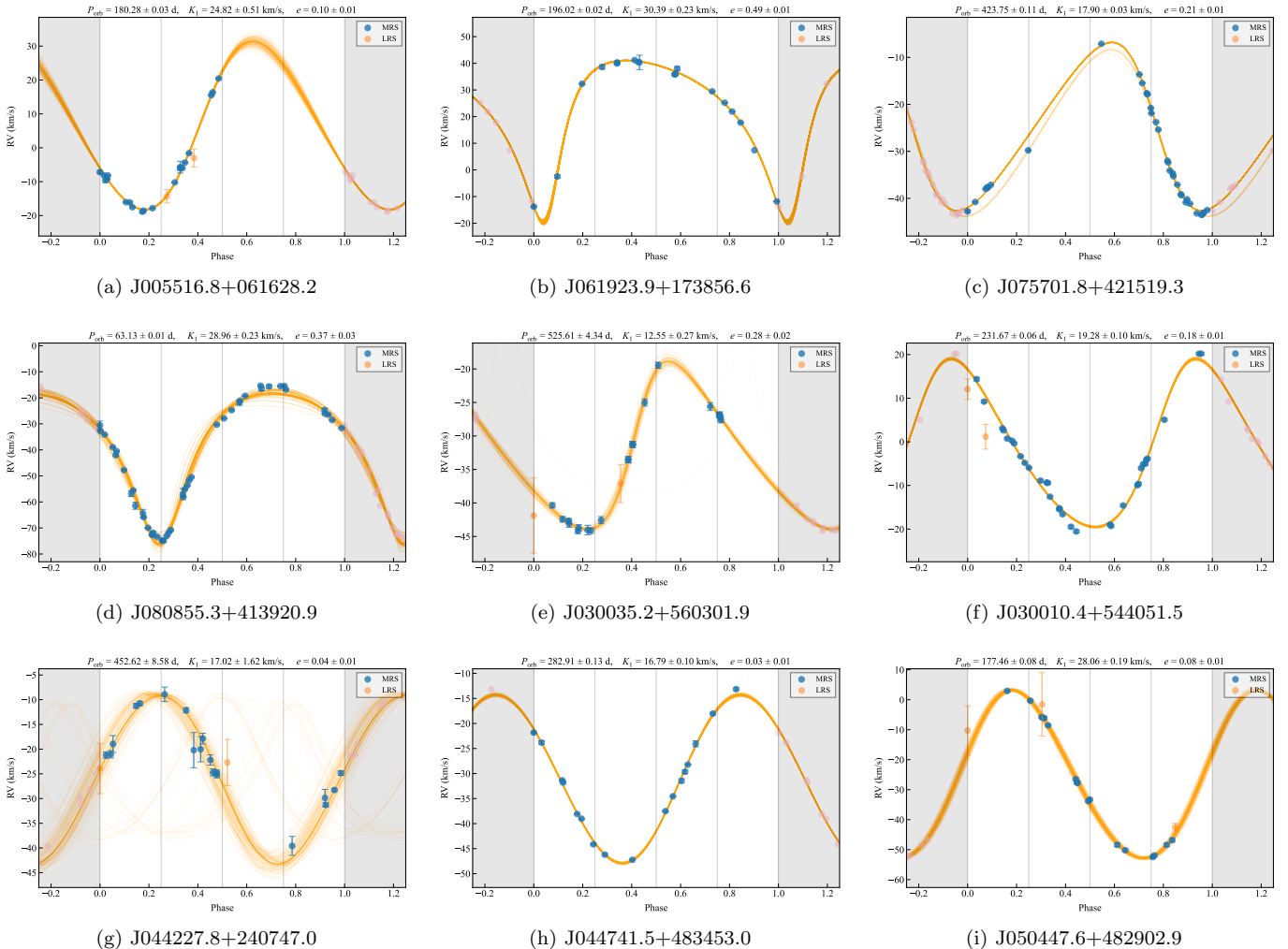
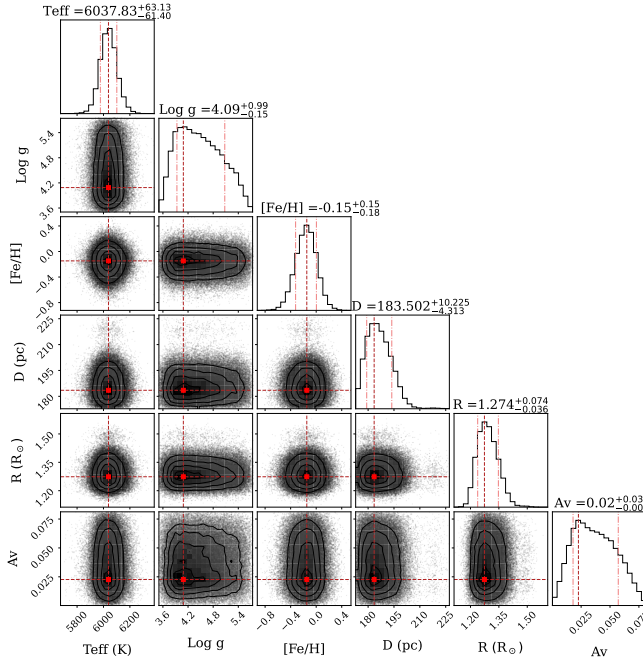


Figure 4. Phase-folded radial velocity curves and best-fit Keplerian orbital solutions for nine representative binary candidates from our sample. For each panel, blue circles denote the MRS observations, orange circles denote the LRS observations. The solid orange line indicates the median fit, while the shaded region represents the bundle of possible orbits consistent with the posterior distribution.

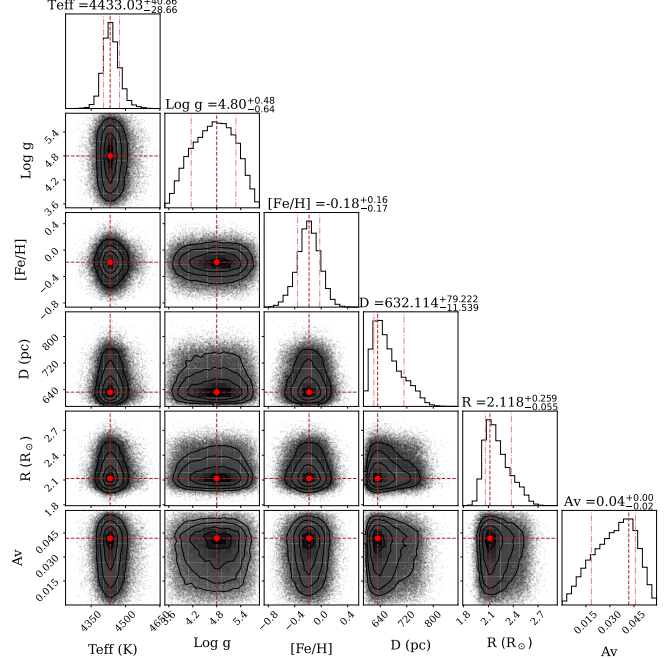
B. SED FITTING

This section details the technical nuances of our SED modeling and the stringent criteria for photometric data selection. To ensure the fidelity of the derived stellar parameters, we implemented a targeted data-filtering strategy. While *astroARIADNE* can incorporate a wide array of catalogs, we found that certain datasets (most notably SDSS and TESS) frequently introduced systematic biases for our bright candidate stars possibly due to saturation effects and pixel-level blending. Consequently, these were excluded to mitigate noise in the Bayesian model-averaging process.

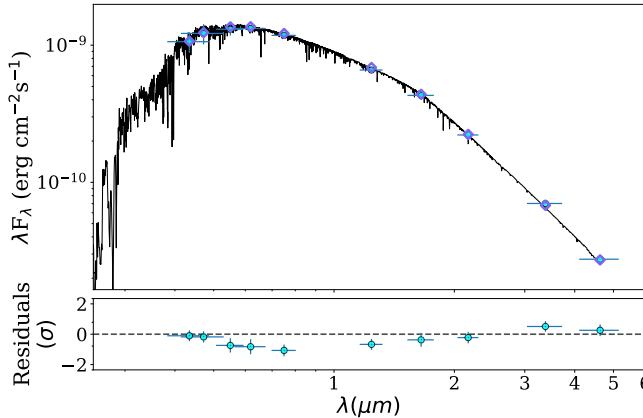
Instead, our analysis prioritized a core set of high-reliability, multi-band catalogs to ensure broad panchromatic coverage. We utilized the Galaxy Evolution Explorer (GALEX) for ultraviolet constraints, the AAVSO Photometric All-Sky Survey (APASS) for the optical regime, and the Two Micron All-Sky Survey (2MASS) coupled with the Wide-field Infrared Survey Explorer (WISE) for the near- and mid-infrared. This strategic selection effectively brackets



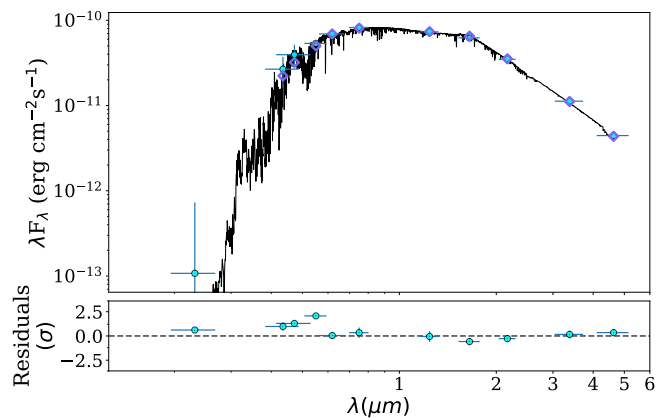
(a) Corner plot for J084437.0+194238.9



(b) Corner plot for J084423.8+152520.8



(c) Best-fit SED for J084437.0+194238.9



(d) Best-fit SED for J084423.8+152520.8

Figure 5. Representative SED fitting results and posterior probability distributions (corner plots) for two candidates. In the SED panels, the black line represents the best-fit model, and the colored points denote the observed photometry. The corner plots show the correlations between the derived stellar parameters (T_{eff} , R_1 , $[\text{Fe}/\text{H}]$, and $\log g$).

the blackbody peak of our late-type targets while providing a long lever arm to break degeneracies between effective temperature and interstellar extinction. The resulting SED fits and the associated posterior probability distributions (corner plots) are illustrated in Figure 5, where the highly localized constraints on R_1 and T_{eff} underscore the robustness of our filtered-photometry approach.

C. SUMMARY OF DERIVED PARAMETERS FOR OTHER CANDIDATES

Table 3 and Table 4 list our analysis results for candidates in Class B and Class C, respectively. While these sources also exhibit significant radial velocity variations, their higher stellar densities or lower mass ratios distinguish them from the primary compact object candidates in Class A.

Table 3. Orbital and Physical Parameters of the Candidates in Class B

LAMOST Designation (J2000)	<i>Gaia</i> DR3 source_id	RUWE	P_{orb} (days)	K_1 (km/s)	$f(M_2)$ (M_{\odot})	T_{eff} (K)	R_1 (R_{\odot})	L_1 (L_{\odot})	M_1 (M_{\odot})	$M_{2,\text{min}}$ (M_{\odot})
(1)	(2)	(3)	(4)	(5)	(6)	(7)	(8)	(9)	(10)	(11)
J024859.0+534307.2	453458047208953344	1.65	440.1	15.2	0.145	4146	38.86	395.80	0.98	0.76
J025948.5+544607.7	459393898169205248	1.17	322.4	27.4	0.475	4108	19.63	98.70	1.24	1.54
J030010.4+544051.5	459375584428683648	1.23	231.7	19.3	0.262	5166	6.35	25.62	1.23	1.14
J030035.2+560301.9	459792402416078080	2.34	525.6	12.6	0.280	4125	17.49	79.32	1.22	1.17
J030058.1+533839.1	441271846300359552	1.21	37.6	36.4	0.183	4070	9.72	22.76	1.05	0.88
J031324.7+545919.5	447622629760600960	1.61	291.4	29.3	0.636	4414	49.77	843.61	0.98	1.63
J034116.6+492438.1	249599279929183744	1.22	490.3	20.9	0.445	4266	34.23	351.17	2.30	2.03
J041014.9+533012.6	275234290455134336	1.04	157.7	25.8	0.262	4513	4.64	8.02	1.04	1.04
J043457.8+275049.4	151935365746006912	1.37	545.0	16.5	0.211	4559	14.47	77.60	1.02	0.93
J044227.8+240747.0	146856034341794432	2.89	452.6	17.0	0.227	4734	16.05	113.24	1.08	0.99
J044902.9+473739.0	255694216477122944	1.16	375.4	19.8	0.269	3888	11.95	29.24	1.04	1.06
J045853.1+482528.9	255421468874513408	1.05	31.2	44.9	0.285	4683	10.50	48.16	0.98	1.06
J050208.0+500020.0	256575440687517312	1.14	1088.4	18.6	0.604	4471	17.82	112.90	1.05	1.63
J050259.7+454413.1	206657917727078400	1.03	41.1	45.5	0.393	4657	15.65	103.91	0.96	1.24
J050447.6+482902.9	255262280206054144	1.08	177.5	28.1	0.429	4632	23.27	227.88	1.05	1.35
J050636.5+483830.8	255290523910817024	1.02	227.8	28.8	0.523	4471	41.96	611.15	1.73	1.90
J055223.9+282946.1	3443195600969981440	1.27	56.4	36.1	0.269	4734	15.47	109.97	1.46	1.26
J055726.6+293812.7	3443720037956728704	1.07	197.8	26.6	0.288	4682	11.83	60.82	1.22	1.19
J061815.5+191501.5	3373971899373213696	1.01	151.9	28.0	0.333	4733	9.59	39.91	0.96	1.13
J061923.9+173856.6	3370664224799960960	1.14	196.0	30.4	0.371	4376	17.87	101.72	1.09	1.28
J063343.3+185027.5	3371448618966873472	1.05	38.2	37.8	0.207	4514	13.72	68.54	1.03	0.92
J075701.8+421519.3	922558601519568640	2.69	423.8	17.9	0.217	4699	5.71	14.30	0.97	0.92
J084407.6+121642.6	602226776508211328	1.07	36.2	38.1	0.147	4585	6.23	15.39	0.93	0.74
J091645.3+431251.8	816274447459979776	1.02	152.2	23.8	0.205	4729	10.98	54.14	0.97	0.89

NOTE—Columns (1)–(11): Same as described in Table 1.

Table 4. Orbital and Physical Parameters of the Candidates in Class C

LAMOST Designation (J2000)	<i>Gaia</i> DR3 source_id	RUWE	P_{orb} (days)	K_1 (km/s)	$f(M_2)$ (M_{\odot})	T_{eff} (K)	R_1 (R_{\odot})	L_1 (L_{\odot})	M_1 (M_{\odot})	$M_{2,\text{min}}$ (M_{\odot})
(1)	(2)	(3)	(4)	(5)	(6)	(7)	(8)	(9)	(10)	(11)
J005516.8+061628.2	2553423070392591616	10.35	180.3	24.8	0.117	5429	5.00	19.38	1.83	0.97
J035243.1+251621.8	66896456396598400	5.35	224.0	16.2	0.093	5294	1.37	1.32	0.98	0.62
J044741.5+483453.0	255981326450428160	1.49	282.9	16.8	0.147	4480	12.59	57.08	1.21	0.86
J054945.8+284136.3	3443234942870379520	2.12	415.1	13.7	0.080	4814	3.25	5.14	0.98	0.58
J062027.2+170224.0	3370019425652181760	1.06	406.5	15.9	0.147	4434	24.84	215.43	1.18	0.84
J062749.8+164036.9	3369382602259770240	1.30	295.5	19.3	0.206	4091	45.43	514.42	1.78	1.23
J064430.0+222242.3	3379409980803092992	1.23	462.6	13.4	0.098	4477	12.36	53.51	1.06	0.66
J064915.6+234352.0	3381148682347487104	5.65	248.3	18.5	0.060	4389	0.80	0.21	0.77	0.45
J075559.7+423618.3	922619040299244544	1.00	30.3	28.0	0.062	5848	1.75	3.25	1.03	0.53
J075753.6+400910.1	919859609711334656	1.02	36.0	25.8	0.063	5963	1.45	2.41	0.94	0.51
J080732.3+423044.8	922048977880637952	1.00	102.1	22.4	0.097	5401	2.60	5.25	1.05	0.66
J080859.0+401829.2	921175175374132224	1.14	98.1	22.2	0.091	5654	1.49	2.05	0.98	0.61
J083758.9+120828.8	602921770936175744	1.28	75.4	25.4	0.081	5145	1.45	1.32	0.99	0.59
J083856.2+125631.1	603083575240672128	1.06	169.0	16.8	0.076	5416	1.88	2.71	1.10	0.60
J084607.7+120652.4	602040757180427904	1.31	268.0	17.5	0.120	5360	2.09	3.24	1.07	0.73
J084643.4+101907.1	598512248272932224	1.00	288.3	20.8	0.227	4142	75.91	1516.71	3.59	1.90
J084743.3+135618.3	608495367176895488	1.50	170.6	17.4	0.070	5905	1.33	1.93	1.05	0.57
J084901.7+125128.3	608098791371422848	1.33	925.0	7.8	0.035	5040	11.53	77.44	2.65	0.74
J084940.5+132958.2	608417954686374400	1.23	66.9	26.1	0.111	5441	1.27	1.25	0.91	0.65
J085027.0+114831.3	604962365734255744	1.00	62.6	34.5	0.131	5690	1.72	2.81	1.06	0.76
J085059.2+115636.8	604969748782357888	1.85	205.5	11.3	0.024	5605	1.72	2.83	1.11	0.38
J085413.0+125553.1	605156463895618816	1.04	140.4	18.5	0.055	5679	1.88	3.36	1.07	0.52
J085418.5+110038.2	604615229297129344	1.10	64.8	26.9	0.089	6014	1.13	1.50	1.02	0.62
J085424.0+103016.8	597832307705755264	0.98	33.4	27.8	0.052	5782	2.27	5.21	1.25	0.55
J090321.2+422908.2	816788778383626368	1.24	89.5	20.0	0.066	5636	1.60	2.32	0.95	0.52
J090658.7+435707.3	1009409059357968640	0.96	52.1	25.6	0.073	5885	1.20	1.55	0.95	0.55
J091705.6+415450.4	816137661341669760	1.16	109.3	25.0	0.103	5715	1.46	2.04	1.00	0.66
J104129.6+090143.6	3869073464141494400	0.98	186.7	18.7	0.087	4640	6.56	18.16	0.95	0.59
J104150.7+095125.1	3870291718729769728	0.95	77.2	25.1	0.115	5035	6.54	24.53	2.05	1.03
J104507.4+102053.6	3869678917091008256	1.27	201.5	13.9	0.052	4917	0.92	0.45	0.84	0.44
J104529.1+410936.8	779784302233147008	1.06	141.7	14.4	0.033	5353	2.06	3.14	0.95	0.39
J104542.6+084305.5	3869178948538080384	1.36	146.4	19.0	0.102	4966	0.83	0.38	0.81	0.58
J104912.6+405323.7	779730254364672768	1.09	97.8	24.7	0.110	5523	1.57	2.14	0.96	0.66
J112002.0+033213.7	3811920643571285376	1.20	215.4	18.2	0.093	4905	1.29	0.87	0.95	0.61
J112249.4+024806.9	3810880608650769024	1.29	186.9	17.5	0.093	5695	1.98	3.70	1.07	0.65
J114552.7+351726.7	4031997035561149824	1.27	138.8	22.5	0.147	5055	2.76	4.88	1.15	0.83
J114849.8+344617.1	4031173913668830592	1.30	61.8	30.1	0.080	5109	1.20	0.87	1.08	0.61
J115407.7+335629.9	4027899499321499392	1.35	190.2	16.5	0.070	5729	1.39	1.87	0.98	0.55
J115642.0+362234.5	4031753356296573056	1.19	96.7	21.7	0.075	5831	1.17	1.44	0.86	0.52
J115806.7+352745.1	4031465284249987840	1.84	247.5	13.6	0.063	5403	1.17	1.05	0.98	0.52
J120015.6+342700.2	4028333256658887808	2.64	321.5	12.1	0.056	4590	0.88	0.31	0.78	0.44
J121035.2+474135.8	1546020658419142656	1.87	13.4	44.9	0.122	6335	1.82	4.83	1.32	0.82
J132900.1+513023.8	1559800047369745408	1.45	45.7	32.1	0.151	4921	8.00	33.93	1.20	0.86
J140746.1+454135.6	1505795162949644928	1.20	511.1	13.4	0.096	4742	9.82	44.00	0.98	0.63
J142728.2+453124.5	1494473388638937728	1.79	536.4	14.3	0.154	5136	3.95	9.63	1.29	0.91
J230707.0+352452.3	1914890969694599296	1.09	11.2	44.9	0.101	5809	3.19	10.56	1.40	0.78

NOTE—Columns (1)–(11): Same as described in Table 1.